La Coupole: A SVBRDF measurement device for large and non-planar objects

ANTOINE LUCAT,[†1,3] PIERRE MÉZIÈRES,[†2] FRANÇOIS MARGALL,[2] LOUIS DE OLIVEIRA[2,3], MARJORIE PAILLET[2], ARNAUD TIZON[4], PIERRE BÉNARD[2,3] AND ROMAIN PACANOWSKI[2,*]

[†] Joint first authors
[1] *Institut d'Optique Graduate School,*[2] *Inria, France*
[3] *Université de Bordeaux, France,*[4] *CNRS, France.*
[*] *romain.pacanowski@inria.fr*

Abstract: We present *La Coupole*, a device for measuring SVBRDF of large and non-planar objects whose ultimate goal is to reproduce the appearance of the object as it would be seen under any lighting conditions and as perceived by the human eye at a distance of approximately 30 cm minimum; in particular, to provide virtual tools for visualization, inspection, and diagnosis of ancient and fragile objects. With this in mind, we compare two BRDF representations without prior assumptions (Spherical Harmonics and Radial Basis Functions) to reconstruct any BRDF and a third one, a GGX microfacet-based model. The paper also provides details of the geometric and radiometric calibration process, along with an in-depth study of their respective uncertainties.

1. Motivation and Related Work

Digitization of real-world objects has many applications ranging from Cultural Heritage (preservation, virtual exhibits) to the manufacturing industry where a virtual mock-up needs to be validated before the mass production launches. The result of the digitization is a digital twin that should look as realistic as the original object to a human observer. To produce digital twins, the appearance of the original object must be acquired. Appearance is the combination of distinct, but intertwined, intrinsic quantities: the shape and the optical properties of the artifact.

In this paper, we introduce a new measurement device, named *La Coupole*, that has been conceived to acquire the appearance of large objects with the following two objectives: **(i)** be as accurate as the human visual system, **(ii)** maintain metrological traceability. *La Coupole* combines measurements from a 3D laser scanner, which acquires the shape of the object, and a DSLR camera, which takes pictures in a controlled lighting environment to provide reflectance measurements.

Over the past twenty years, other acquisition systems have been developed to acquire the appearance of objects. Since our acquisition device aims at measuring spatial variations of reflectance, we purposely focus on the Spatially-Varying Bidirectional Reflectance Distribution Function (SVBRDF). BRDF measurement devices (more or less automated) have been developed since the 1960s. With the development of digital photography, measurement devices for BRDFs have become imaging systems (*e.g.*, [1, 2]). Recent and comprehensive overviews of BRDF measuring instruments are presented by Weinmann and Kleiny [3] as well as Guarnera *et al.* [4]. It is worth noticing that, without imaging technologies, it would be too time-consuming to measure an SVBRDF densely, even for small-sized objects. Mc Allister [5] and Sattler *et al.* [6] were among the first to measure a nSVBRDF **on a planar surface** using a camera. Their systems are quite slow due to the many mechanical movements that are needed to orient the material sample. To overcome this limitation, recent systems (*e.g.*, [7]) are doing acquisition in parallel (a.k.a. multiplexing) by adding several cameras and light sources.

However, a major limitation remains for appearance acquisition. Objects (*e.g.*, museum artifacts, automotive parts) are rarely planar. Consequently, more recent systems (*e.g.*, [8–11])

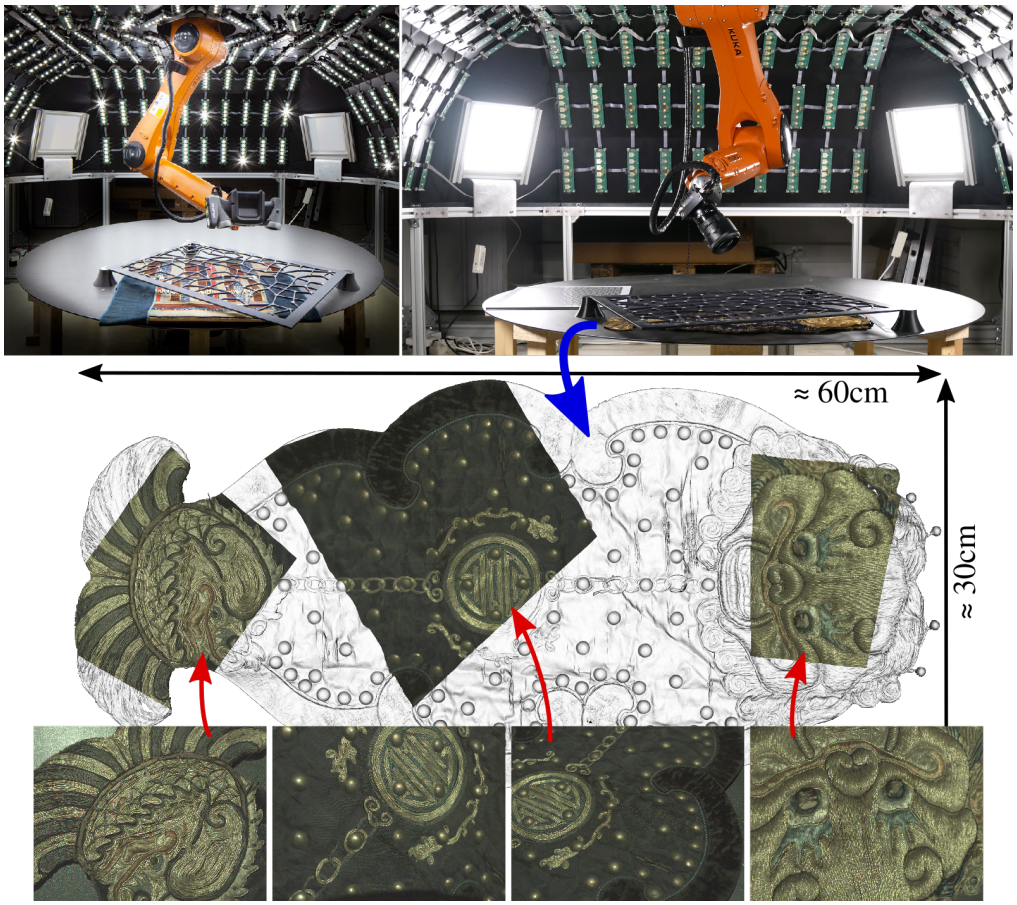

Fig. 1. La Coupole and its two measurement configurations. **Top left:** The 3D scanner is mounted on the robotic arm to acquire the shape (geometry) of the object.**Top right:** after the acquisition of the shape, a high-speed camera is mounted on the robotic arm to measure the SVBRDF with 1080 LEDs. The calibration process determines the acquisition parameters (*e.g.*, the mesh position and camera position and rotation), which allows projecting each photo onto the mesh (**Bottom**).

combine structured lighting to acquire the shape of the object with multiple light sources and/or cameras. In particular, the solutions introduced by Schwartz [9, 10] and by Köhler [11] are related to ours since they rely on a dome to place multiple light sources and cameras. However, the resolution of the view direction they obtain is inferior to ours since the number of cameras is fixed (e.g., in [10]). In summary, previous dome-based systems are limited in terms of camera resolution and object size.

The object size limitation is mainly related to the choice of the camera field of view. It is a compromise between the spatial resolution of the measurement and the object size. In practical terms, for *La Coupole* imaging 1 m^2 at a resolution of 100 µm would require a sensor of 100 million pixels per view direction and an adequate lens to have sufficient depth-of-field, resulting in an overly expensive camera. The system proposed by Holroyd *et al.* [8] is quite original: two robotic arms are moving around the object, each arm carrying a camera and a video projector, which is used either to project a structured pattern or to illuminate the object. The main disadvantage of the system is its relative slowness, and the maximum size of the object is

also limited by the camera's field of view.

Recently, Garcès et al. [12] have introduced a dome system, with a wingspan of 30 cm, specialized for a small textile patch of 11x11cm. The acquisition is done under 127 LED and is constrained to 3 camera positions. As done in VarIS [13], they assume a planar geometry and a SVBRDF model with a normal map, and optimize the geometry and the SVBRDF at the same time. In other words, as usually accomplished by photogrammetric-based approaches(*e.g.*, [14, 15]), shape and reflectance measurements are intertwined and tracking the uncertainties of the shape or the SVBRDF is never established.

Our solution, to combine measurements of different equipment while keeping track of the uncertainties, is presented in more detail in Section 4 where we give more insights into the calibration procedure and in Section 6.1, where we provide a comprehensive analysis of the radiometric and geometric uncertainties of the measured SVBRDF. Furthermore, instead of assuming a BRDF model, we evaluate two mathematical representations (Spherical Harmonics and linear Radial Basis Functions, Sec.5) to approximate the measurements and reconstruct the BRDF as a continuous function, and compare (Section 6) them to a classical BRDF model (GGX) based on the micro-facet theory [16]. Finally, we conclude by discussing (Section 7) the different limitations and sketch future work directions in terms of calibration and uncertainty reduction, as well as the data processing pipeline.

2. Acquisition Setup

The aforementioned constraints led us to conceive and build *La Coupole* (*cf.* Fig. 1) that consists mainly in the following parts:

The support for the material sample is a disk of 1.48 m diameter and 0.3 mm thickness made of black anodized Dibond. The Dibond has the advantage of being lightweight and the anodization process makes the support more absorbing, thus reducing parasite lighting.

The 6-axis robot, KUKA Model Agilus kr10r1100sixx C, is used to move either the camera or the 3D scanner. With a maximum reach of 1.1 m, the robot can reach all positions of the support. According to the manufacturer, its pose repeatability is 30 µm.

The 3D laser scanner, HandyScan 700 (Creaform), is used to acquire the shape (geometry) of the sample (see Fig. 1 left). The manufacturer announces a resolution of 50 µm (distance between two points) with an accuracy of 30 µm (*i.e.*, the position of a point measured from the scanner is known up to 30 µm). The speed of the scanner (480 000 points per second) makes it very competitive compared to photogrammetric approaches: a 1 m^2 surface can be acquired in 15 minutes. From a metrological point of view, the HandyScan precision is traced back to the meter standard delivered by the French *National Institute of Metrology*. The scanner needs to see retro-reflective stickers to orient itself. These stickers are pasted on a calibration target positioned around or above the material sample.

The lighting system consists of 1080 LEDs and 4 flat white LED panels. For cultural heritage applications, LEDs have the key advantage of not emitting any UV radiation, which would degrade textile artifacts, for example. The four LED Panels (manufactured by Airis) generate an almost perfect uniform lighting and serve during the calibration step to calibrate the spatial sensitivity of the camera sensor (see below). The 1080 LEDs are distributed across 180 electronic Printed Circuit Boards (PCBs) mounted on an aluminum structure that surrounds the support. Each LED is 7 mm square and emits around 1800 lumens. An LED can be turned on for at least 1 ms (electrical current rise constraint) and up to 2 seconds (heat dissipation constraint).

An electronic control box allows us to control each LED independently and also triggers the camera via a physical cable. This hardware triggering mechanism ensures good synchronization performance and high-speed acquisition.

The camera (Ximea Model CB120CG-CM) is used to acquire the optical properties of the material sample by taking one picture every time an LED is turned on. The camera can capture 100 frames per second. Its RGB-CMOS sensor size is 4096×3072 pixels, where each pixel size is 5.5 µm, with a good signal-to-noise ratio of 42 dB. The **lens** in front of the camera is a 35 mm Sigma HSM Art. The minimal focus distance is stated to be 30 cm. With a lens aperture set to at least $f/8$, we can achieve the one-degree angular resolution required to mimic the human eye. The combination of the Sigma lens and the Ximea sensor leads to an imaging system that acquires a $14.5 \times 19.3\,\mathrm{cm}^2$ rectangular surface where each image pixel, at normal incidence, represents a square of 47 µm on a side in object space.

In summary, *La Coupole* can acquire the appearance of an object whose projected wingspan does not exceed 1.4 m and whose height is at most 70 cm. The acquisition is a two-step process where, during the first step, the 3D scanner acquires the object shape and outputs a triangle mesh, whereas during the second step, for each position of the camera, an image is acquired each time an LED is switched on.

3. Measurement Equation

Radiometrically, the BRDF at position $\boldsymbol{x}$ is defined [17] for a pair of infinitesimal outgoing $\boldsymbol{o}$ and incoming $\boldsymbol{i}$ directions, as the ratio of the reflected radiance and irradiance. Applied to our measurement context that uses a DLSR camera, which images the object, and an LED light source, which subtends a finite solid angle, our measurement equation of the spatially varying BRDF (SVBRDF) becomes:

$$BRDF(\boldsymbol{x}, \boldsymbol{o}, \boldsymbol{i}_k) = \frac{L(\boldsymbol{x}, \boldsymbol{o})}{E_k(\boldsymbol{x}, \boldsymbol{n}_x)} \qquad \text{with} \quad L(\boldsymbol{x}, \boldsymbol{o}) \approx \frac{4\,(m+1)^2 \cdot f_\#^2 \cdot V_p}{\pi \cdot A_p \cdot t_e \cdot g(p)} \tag{1}$$

where: $L(\boldsymbol{x}, \boldsymbol{o})$ is the reflected radiance at point $\boldsymbol{x}$ in direction $\boldsymbol{o}$; $E_k(\boldsymbol{x}, \boldsymbol{n}_x)$ is the irradiance at point $\boldsymbol{x}$, with normal $\boldsymbol{n}_x$, due to the k-th LED light source, which main direction is $\boldsymbol{i}_k$ (*cf.* Fig. 2).

Since the BRDF is a relative quantity, we measure the incident irradiance and the reflected radiance in the same radiometric space using the same camera. In the equation above, the pixel value is denoted V_p, A_p is the area of one pixel of the camera sensor, t_e is the exposure time, $f_\#$ is the selected aperture, m is the optical magnification of the lens and $g(p) \in [0, 1]$ represents a flat-field correction that takes into account vignetting and other radiometric effects.

Without absolute calibration, $L(\boldsymbol{x}, \boldsymbol{o})$ unit is $\mathrm{DN\,s^{-1}\,m^{-2}\,sr^{-1}}$ and $E_{\boldsymbol{i}_k}(\boldsymbol{x}, \boldsymbol{n}_x)$ unit is necessarily $\mathrm{DN\,s^{-1}\,m^{-2}}$. We assume that an LED is a rectangular light source that emits uniformly with a cosine angular distribution, which is reasonable according to the LED manufacturer specifications. Under these assumptions, we model the irradiance $E_k(\boldsymbol{x}, \boldsymbol{n}_x)$ using Lambert's irradiance [18]:

$$E_k(\boldsymbol{x}, \boldsymbol{n}_x) = \frac{\Phi_k}{2\,A_l} \left\langle \mathbf{G}_f(\boldsymbol{x}, \boldsymbol{l}_k), \boldsymbol{n}_x \right\rangle \left\langle \boldsymbol{n}_k, -\boldsymbol{i}_k \right\rangle \tag{2}$$

where: $\langle\,,\rangle$ represents the dot product between two vectors; $\boldsymbol{l}_k$ is the position of the center of the k-th LED; A_l is the area of an LED; Φ_k is the power of the k-th LED; $\boldsymbol{n}_k$ is the k-th LED surface normal (*i.e.*, its orientation and $\langle \boldsymbol{n}_k, -\boldsymbol{i}_k \rangle$ corresponds to the cosine emission of the LED); $\mathbf{G}_f(\boldsymbol{x}, \boldsymbol{l}_k)$ is a geometrical and vectorial quantity defined in the supplemental document [19].

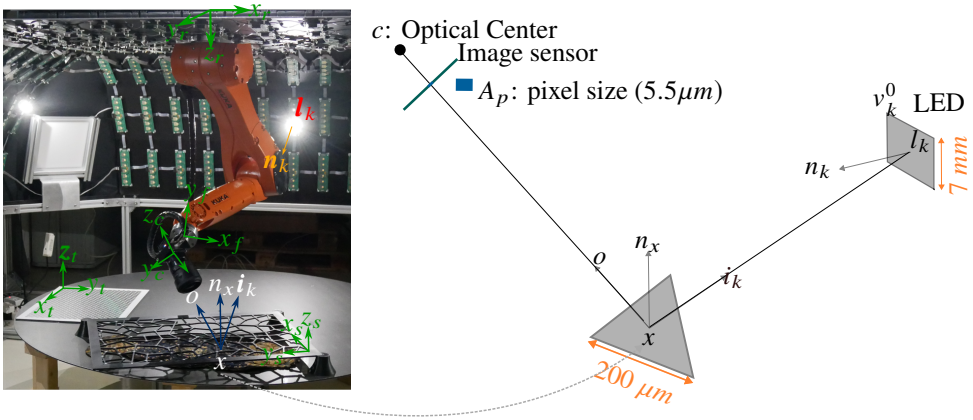

Fig. 2. **Left.** The different coordinate systems: $(\boldsymbol{x_s}, \boldsymbol{y_s}, \boldsymbol{z_s})$ for the 3D scanner, $(\boldsymbol{x_t}, \boldsymbol{y_t}, \boldsymbol{z_t})$ for the ChArUco board, $(\boldsymbol{x_c}, \boldsymbol{y_c}, \boldsymbol{z_c})$ for the camera, $(\boldsymbol{x_f}, \boldsymbol{y_f}, \boldsymbol{z_f})$ for the robot flange, and $(\boldsymbol{x_r}, \boldsymbol{y_r}, \boldsymbol{z_r})$ for the robot base. **Right**. Illustration of the different mathematical notations used in the paper. The optical center $\boldsymbol{c}$ is the center of the camera coordinate system. The triangle, whose size is much smaller than an LED, belongs to the mesh acquired thanks to the 3D scanner.

Therefore, for a given observation direction and a given LED, our measurement equation becomes:

$$BRDF(\boldsymbol{x}, \boldsymbol{o}, \boldsymbol{i}_k) = \frac{8\,(m+1)^2 \cdot f_\#^2 \cdot V_p}{\pi \cdot A_p \cdot t_e \cdot g(p)} \cdot \frac{A_l}{\Phi_k \langle \mathbf{G}_f(\boldsymbol{x}, \boldsymbol{l}_k), \boldsymbol{n}_x \rangle \cdot \langle \boldsymbol{n}_l, -\boldsymbol{i}_k \rangle} \tag{3}$$

As shown by Eq. 3, one needs to calibrate for radiometric quantities (the power of an LED Φ_k, the flat field function g) as well as geometrical quantities (*e.g.*, $\boldsymbol{o}, \boldsymbol{x}, \boldsymbol{i}_k = \frac{\boldsymbol{l}_k - \boldsymbol{x}}{||\boldsymbol{l}_k - \boldsymbol{x}||}, \boldsymbol{l}_k, \boldsymbol{n}_k$).

4. Calibration Procedure

4.1. Geometrical Calibration

The definition of the SVBRDF requires the geometrical quantities $\boldsymbol{x}, \boldsymbol{o}, \boldsymbol{l}_k$ to be expressed in the same coordinate frame. In our setup, only the coordinate system $(\boldsymbol{x}_r, \boldsymbol{y}_r, \boldsymbol{z}_r)$, attached to the base of the robot, is temporally invariant. To express all quantities in the robot base frame, we calibrate the geometrical quantities following three main steps:

1. Calibration of the optical center of the camera with respect to the robot base frame, which requires choosing a camera model and calibrating for intrinsic (effective focal length, distortions, focus distance, etc.) and extrinsic parameters of the camera.
2. Calibration of the position of each LED with respect to the robot base frame.
3. Calibration of the rigid transformation (called "mesh-to-robot" in the following) between the frame of the mesh, obtained from the 3D scanning process, and the robot base frame.

Once the camera, the LEDs, and the mesh are expressed in the same frame, for each pixel of an acquired image, we trace a ray to find the intersection with a triangle of the mesh, and then deduce the viewing $\boldsymbol{o}$ and LED direction $\boldsymbol{i}_k$. The local surface normal, $\boldsymbol{n}_x$, is computed from the mesh vertices.

Camera Intrinsic and Extrinsic Parameters calibration. For each focusing distance, we calibrate the intrinsic and extrinsic properties by taking between forty and sixty images of

the ChArUco calibration board. With these images, we apply the method from Zhan [20], implemented in OpenCV [21], for estimating intrinsic and extrinsic parameters of a thin-lens camera model. For each image, we obtain the camera position in the ChArUco frame ($(\boldsymbol{x_t}, \boldsymbol{y_t}, \boldsymbol{z_t})$ in Fig. 2).

Camera Position calibration. To estimate the camera position in the robot frame, we apply a simplified hand-eye(e.g., [22]) calibration procedure, yielding a positioning uncertainty of 300 µm. The hand-eye calibration procedure takes advantage of the fact that the rigid transformation between the robot flange center and the center of the camera frame (*i.e.*, the optical center) is constant no matter the position of the robot.

LED Position calibration. Once the camera position is calibrated *w.r.t.* the robot frame, we take 6 images of each switched-on LED and perform an optical triangulation by tracing camera rays for each image, and finding the camera rays minimal intersection distance. As detailed in the supplemental document [19], the positioning accuracy of each LED center is 700 µm whereas the uncertainty associated with its normal is at worst 0.21°.

Mesh-to-robot rigid transformation calibration. To establish the transformation between the scanner frame $(\boldsymbol{x}_s, \boldsymbol{y}_s, \boldsymbol{z}_s)$ and the robot base, we introduce a new procedure that seeks to establish the rigid transformation between the positions of the 3D scanner stickers defined in the scanner frame, and the position of the stickers photographed by the Ximea camera. Our new procedure is based on two algorithms: **(i)** an algorithm that operates in image space and detects the gray stickers of the ChArUco board. This algorithm uses both the shape and color properties of the stickers; **(ii)** an algorithm that operates in 3D space and establishes the best match between the triangles formed by the stickers and the associated points. The uncertainty of the estimated rigid transformation between frames $(\boldsymbol{x}_s, \boldsymbol{y}_s, \boldsymbol{z}_s)$ and $(\boldsymbol{x}_r, \boldsymbol{y}_r, \boldsymbol{z}_r)$ is at most 100 µm. The entire geometric calibration procedure is detailed in the supplemental document [19].

4.2. Radiometric Calibration

As done classically, the camera is calibrated to account for vignetting by estimating the flat field g. This is done by imaging the white LED panel and by fitting a mathematical model to filter out the noise. The response curve of the sensor is also calibrated by taking multiple images for different exposure times of a static scene. Our additional calibration results [19] show that our camera exhibits a linear response.

The power of the LEDs (Φ_k in Eq. 3) is obtained from several photos of a spectralon target, by averaging the pixels seen by the spectralon and illuminated by different LEDs. By using the same camera between the spectralon calibration photos and the photos used to extract the SVBRDF of the measured objects, Eq. 3 can be simplified. The equations used in practice for the data processing pipeline (Sec. 5) and their derivations are given in the supplemental document [19].

5. Data Processing Pipeline

In this section, we focus on single-view and multi-light acquisition. In other words, we only perform BRDF slice acquisition as the camera direction is fixed for every point on the object. Section 5.1 describes the construction of our SVBRDF and the processing of images to extract SVBRDF samples. Since the extracted data are angularly sparse, we need a continuous representation to synthesize a new image for a non-acquired light direction. Therefore, using different material samples, we analyze three types of representations: Spherical Harmonics (Sec. 5.2), Radial Basis function (Sec. 5.3), and a microfacet-based BRDF model using the GGX [23] distribution (Sec. 5.4).

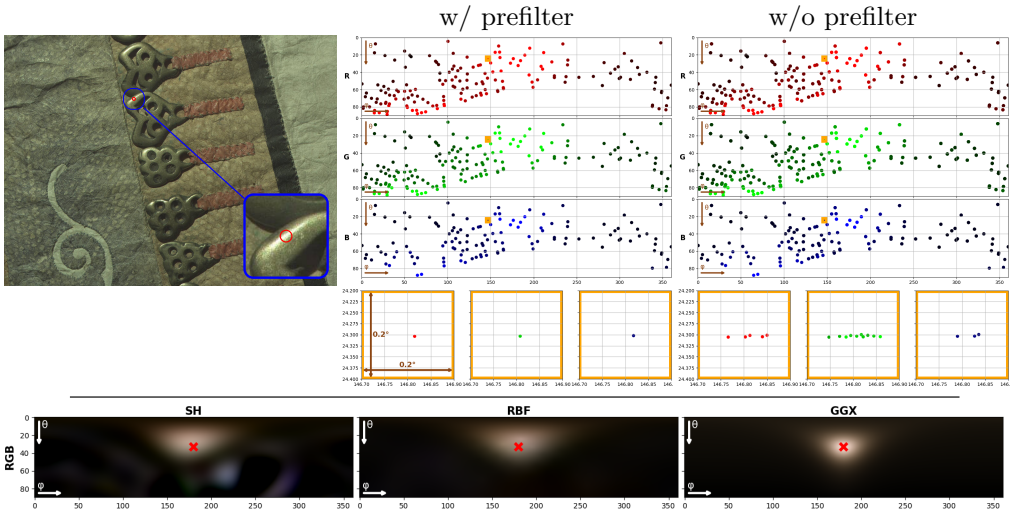

Fig. 3. Visualization of samples (latitude-longitude parameterization) from a triangle located within the red circle (top). Pre-filtering avoids redundancy of samples that are too close together angularly (around 0.1°). The sample numbers for the RGB channels are, respectively, 168, 170, 129 with the prefilter and 770, 1505, 325 without the prefilter. The RGB reconstruction using the SH and RBF shows that the specular peak in the measurements is slightly offset from the mirror direction (red cross) (bottom).

5.1. From Acquired Images to BRDF data

To extract BRDF samples from the images, each pixel (using RAW images encoded with GBRG Bayer pattern) is processed and converted into a BRDF value (Eq. 3). Hence, each pixel corresponds to a single RGB color channel, yielding three separate sets of samples (one per channel). Since this paper is limited to the study of fixed viewpoint, storing a triplet is sufficient: $\theta_{\boldsymbol{i}}$, $\theta_{\boldsymbol{o}}$, $\Delta\phi = |\phi_{\boldsymbol{i}} - \phi_{\boldsymbol{o}}|$, where $\boldsymbol{i}$ corresponds to the light input direction and $\boldsymbol{o}$ is the view output direction. The reflectance value f is also stored, and all these parameters are stored in a single-precision floating-point format. We remove too grazing samples ($\theta_{\boldsymbol{i}} > 89°$), this choice discussed in Section 6.4.

We apply a 2% exposure threshold to reject pixels that are underexposed or overexposed. Thanks to the robot 3D model, a shadow mask for the robot arm is computed during the acquisition; hence, pixels belonging to these shadow areas are removed. However, shadows cast by the cables remain hard to predict. The pixel value threshold alleviates this problem and is discussed further in Section 6.4. In this paper, each dataset corresponds to N photos taken, at fixed exposure time, from the same viewpoint and only the LED position varies between each picture.

BRDF Samples are obtained by casting rays from photo pixels to identify the triangle that is "seen" by the pixel. Considering a single photo (a single LED lit) and since the triangles are small compared to the distance between the triangle and the camera, or between the triangle and the LED, this creates samples that are angularly close together when several pixels are linked to the same triangle (see the theoretical analysis in the supplemental document [19]). This angular redundancy is avoided by adding a sample pre-filtering step (Fig. 3).

5.2. From BRDF data to Spherical Harmonics (SH) representation

Any spherical function f can be represented by a weighted sum of spherical harmonics Y.

$$f(\theta,\phi) = \sum_{l=0}^{+\infty} \sum_{m=-l}^{l} \mathbf{F}_l^m \, Y_l^m(\theta,\phi) \approx \sum_{l=0}^{n} \sum_{m=-l}^{l} \mathbf{F}_l^m \, Y_l^m(\theta,\phi) \; . \tag{4}$$

where $\mathbf{F}$ is a vector of coefficients. The index l plays the role of an angular frequency: higher values of l correspond to higher-frequency components on the sphere. This representation is exact only when an infinite number of basis functions is used. When using a finite number of SH, the reconstruction is bandlimited, with a band limit equal to n. In practice, this means that all SH components with $l > n$ are abruptly discarded. Such a sharp truncation in the SH frequency domain introduces a discontinuity in the spectrum, which produces oscillations in the reconstructed signal, commonly called *ringing*, analogous to the *Gibbs phenomenon*. The oscillations are stronger when the reconstruction band limit is small compared to the band limit of the projected signal [24]. From equation 4, the coefficient vector $\mathbf{F}$ can be obtained by writing a minimization problem solved by least squares: $\|\mathbf{Y}\mathbf{F} - F\|^2 + \lambda \, \|\Gamma\mathbf{F}\|^2$, where Γ is the Thikonov matrix and λ control the amount of regularization ($\lambda = 0.1$ by default). Thus, the least squares system is solved for each triangle in the mesh.

5.3. From BRDF data to Radial Basis Function (RBF) representation

The RBF representation of our measurements is a linear combination of radial-basis functions, such as

$$BRDF_{RBF}\,(\boldsymbol{x},\boldsymbol{o},\boldsymbol{i}) = \sum_{n=0}^{N_{\boldsymbol{x}}} \omega_{\boldsymbol{x},n} \, K\left(\|(\boldsymbol{o},\boldsymbol{i})\,;(\boldsymbol{o},\boldsymbol{i})_n\|\right) \tag{5}$$

where:

- $\|\cdot\,;\cdot\| : \mathbb{S}^2_+ \times \mathbb{S}^2_+ \to \mathbb{R}_+$ is the distance function between two bidirections, one $(\boldsymbol{o},\boldsymbol{i})$ being the argument passed to $BRDF_{RBF}$, the other $(\boldsymbol{o},\boldsymbol{i})_n$ being one bidirection of the interpolant;
- $K : \mathbb{R}_+ \to \mathbb{R}$ is the kernel, a radial basis (linear in this paper) function centered on a given bidirection $(\boldsymbol{o},\boldsymbol{i})_n$;
- $\{(\boldsymbol{o},\boldsymbol{i})_n\}_{n=0}^{N_{\boldsymbol{x}}}$ is the set of all bidirections used in the interpolant associated with the $\boldsymbol{x}$ position;
- $\boldsymbol{\omega_x}$ is the vector of size $N_{\boldsymbol{x}}$ containing all the weights associated with each radial-basis function of the interpolant, each one centered on a given bidirection $(\boldsymbol{o},\boldsymbol{i})_n$.

The distance function $\|\cdot\,;\cdot\|$, depending on its definition, allows us, on the one han,d to represent the bispherical topology $\mathbb{S}^2_+ \times \mathbb{S}^2_+ \to \mathbb{R}_+$ of the BRDF, but also some of its properties, such as bilateral symmetry (*i.e.*, with respect to the plane of incidence) or Helmholtz reciprocity.

To use the model, the weights need to be computed, which is done by solving the linear system $\mathbf{K}\,\boldsymbol{\omega} = \mathbf{f}$, where:

- $\mathbf{K}$ is the kernel matrix of size $(N_{\boldsymbol{x}}, N_{\boldsymbol{x},m})$, each element defined as $K_{i,j} = K(\|(\boldsymbol{o},\boldsymbol{i})\,;(\boldsymbol{o},\boldsymbol{i})\|)$;
- $\boldsymbol{\omega}$ is the vector of size $N_{\boldsymbol{x}}$ containing all the weights associated to every RBF bidirection;
- $\mathbf{f}$ is the vector containing the input measured data associated with the position $\boldsymbol{x}$, of size $N_{\boldsymbol{x},m}$.

The supplemental document [19] details how non-negativity and extrapolation to large angles are handled.

5.4. From BRDF data to Microfacet GGX BRDF Model

Cook and Torrance [25] model the optical response as a set of Fresnel mirrors, called microfacets, and thus define specular reflections as the product of three functions: D, the distribution of

microfacet normals, F, the Fresnel term, and G, the shadowing term between microfacets. The GGX model by Walter *et al.* [23] intoduces an analytical formulation to compute the terms D and G. The complete BRDF model used in this paper is the sum of a Lambertian reflection and the specular GGX model:

$$f_{\text{GGX}}(\boldsymbol{i},\boldsymbol{o}) = \underbrace{\frac{k_d}{\pi}}_{\text{Diffuse}} + \underbrace{\frac{D_\alpha(\boldsymbol{h})F(\boldsymbol{o},\boldsymbol{h},\eta)G(\boldsymbol{i},\boldsymbol{o},\boldsymbol{h})}{4(\boldsymbol{n}\cdot\boldsymbol{i})(\boldsymbol{n}\cdot\boldsymbol{o})}}_{\text{Specular}} \tag{6}$$

where $\boldsymbol{n}$ is the surface normal, $\boldsymbol{h} = \frac{\boldsymbol{i}+\boldsymbol{o}}{\|\boldsymbol{i}+\boldsymbol{o}\|}$ is the half vector, η the index of refraction (RGB value), α the roughness of the surface, and k_d is an RGB value, yielding a BRDF model with 7 coefficients. The fitting is performed with the Levenberg-Marquardt algorithm implemented in the Eigen library [26] using an error metric similar to one introduced by Löw *et al.* [27].

6. Results

This section presents the results obtained for the acquisition and reconstruction of the SVBRDF. We first summarize the main sources of uncertainty affecting the BRDF measurements (Sec. 6.1). We then introduce the results obtained with single-view and multi-light datasets, where the reflectance function is estimated at the triangle level and represented using SH, RBF, and GGX models. The sampling characteristics of the reflectance measurements are analyzed in section 6.2. Next, the three continuous representations are compared (Sec. 6.3). Finally, section 6.4 examines the influence of the various parameters that guide the entire processing pipeline.

Each dataset used here corresponds to approximately 300-500 photos (where each corresponds to a single LED being lit) and approximately 500,000 to 1,000,000 triangles are visible in each viewpoint of the datasets. Complementary information on the datasets is provided in the supplemental document [19]. All tests conducted in this paper are performed on a computer with an Intel® Xeon(R) W-2155 CPU @ 3.30GHz × 20 cores, and data are stored on NVME.

6.1. Uncertainty Summary

We conducted a comprehensive uncertainty analysis (see also supplemental document [19]) of our BRDF acquisition system by propagating all identified uncertainty sources through the full measurement model using Monte-Carlo sampling [28]. This evaluation encompasses both the angular uncertainties in the incidence and observation directions, as well as the radiometric uncertainty in the BRDF values.

For angular uncertainty, we compute the variance of the directional spread induced by the finite size of the LEDs, triangles, and pixels. Across our complete dataset, both incidence and observation directions are found to be stable within approximately $\pm 0.5^\circ$, owing to the large LED–triangle and pixel–triangle distances compared to the small triangle size.

For radiometric uncertainty, we evaluate the full probability distribution of each BRDF measurement. We further analyse the global distributions of the asymmetric uncertainty bounds across the entire dataset. These distributions reveal that:

- in the best configurations, radiometric uncertainty can be as low as $[-1.06\,\%; +1.23\,\%]$;
- 50% of all measurements lie below $[-10.66\,\%; +14.00\,\%]$ at 68% confidence;
- 95% of all measurements lie below $[-15.23\,\%; +22.42\,\%]$ at 68% confidence.

A source-wise sensitivity analysis shows that most uncertainty sources are negligible. Two contributions dominate:

1. geometric uncertainty on triangle vertices (caused by scanner 3D accuracy limit of 30 µm), which alone accounts for a reduction of 57.22 % to 74.01 % of the total uncertainty when removed;

2. camera pixel-value uncertainty, contributing to a global reduction of 5.6 % to 12.5 % when removed.

6.2. BRDF Samples Analysis

Angular prefiltering avoids sample redundancy (Sec. 5.1) (Fig. 3). Depending on the case, not applying pre-filtering multiplies the number of samples by approximately 2 to 9. This has an important cost in terms of storage and computation time, specifically for the continuous representations computations (SH, RBF, or GGX) for all triangles, without improving the quality of the results. We typically observe a greater spread of the samples in ϕ than in θ. This is because the spread in θ is calculated in the space of the plane defined by the normal and the sample direction, so in this plane, the distance between the LED and the triangle is very large compared to the size of the triangle, which implies a small spread. For ϕ, the spread is calculated in tangent space, so the projection of the center of the LED on the tangent plane can be very close to the triangle, causing a large spread of samples. An illustration is provided in the supplemental document [19], along with a more in-depth theoretical analysis of the angular spread of the samples.

Angular uncertainty. The reconstruction of the specular lobe is slightly shifted (with SH and RBF) from the expected main reflection direction (mirror direction) (Fig. 3). This is mainly due to the fact that only an approximation of the surface is available, so the uncertainty about the local surface coordinates is reflected in the direction of the samples, thus creating directional uncertainty. Note that this discrepancy does not appear with GGX, because the model enforces the main reflection lobe to be reconstructed in the mirror direction, which is not the case with SH or RBF.

Memory cost and timings. In terms of memory usage, we typically observed sample sets of around 5-15 GB with angular prefiltering (30-60 GB without) for meshes natively acquired by 3D scanner. The meshes we process range from 1 million to 40 million triangles in total, corresponding to file sizes of approximately 25 MB to 1 GB. For each individual viewpoint, the portion of mesh involved typically contains 500,000 to 1 million triangles, amounting to about 9 MB to 17 MB. In terms of computational cost, the samples are exported in approximately 100-200 seconds using approximately 300 photos.

6.3. Comparisons of the three continuous representations

This section compares the results obtained from the three representations defined in Section 5. As shown in Fig. 4, SH and RBF behave similarly during image reconstruction, whereas the GGX model tends to produce more error. However, note that in our experiments, we fitted the three models (SH, RBF, and GGX) to spherical slices of the BRDF. SH and RBF approximations can only reproduce the fitted slice, since they are general-purpose function approximations, whereas the parametric GGX model retains the physical formulation of the BRDF quantity. Therefore, fitting the GGX model to a single slice permits generating an image from a new viewpoint, whereas SH and RBF are not suited for this application case.

Image generation process and comparison method Once the SH, RBF, or GGX coefficients have been obtained for each triangle in the dataset, a synthetic image, under measured or novel lighting conditions, can be generated since we have an estimation of the BRDF for each triangle of the mesh (Fig. 5) [29]. To fairly compare between the acquired photos and the renderings generated with the SH, RBF, and GGX models, the images are generated at the same initial resolution (4096×3072) as the photos and following the same Bayer pattern. Then the

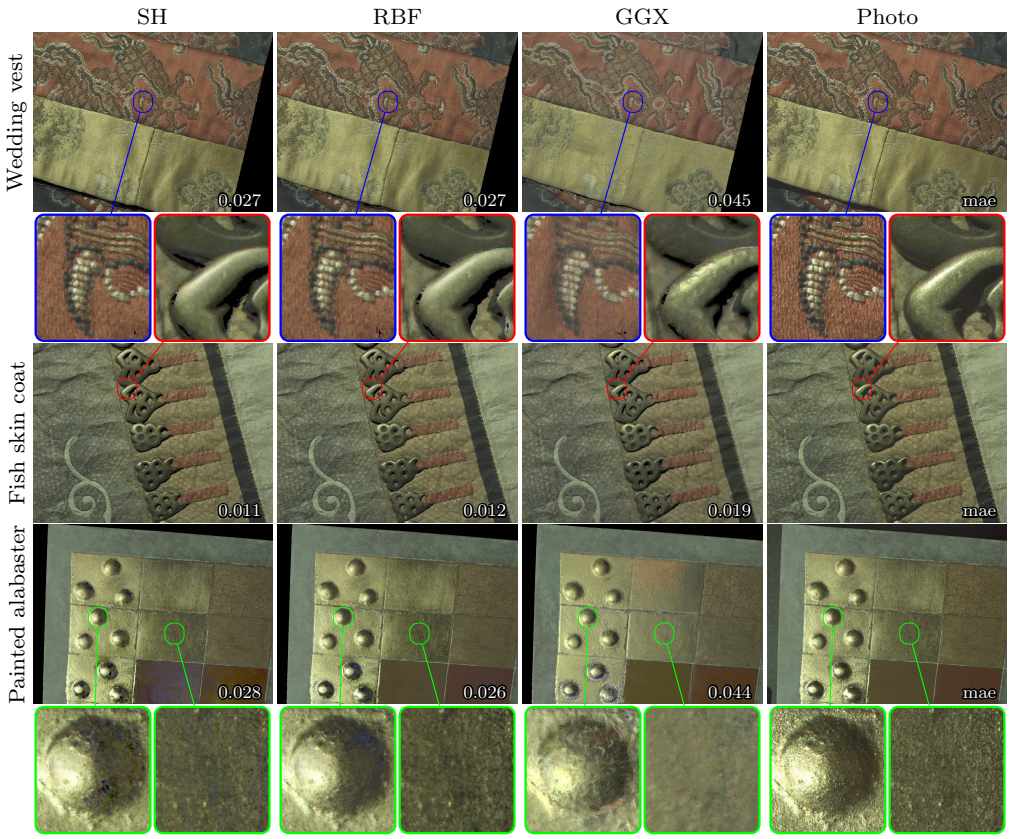

Fig. 4. Reconstruction of a photo using the different continuous representations: SH, RBF, and GGX. SH and RBF each use 100 coefficients per RGB color channel and produce very similar results, whereas GGX tends to produce more errors, which is particularly noticeable in the Mean Absolute Error (MAE)

photographs and renderings are demosaiced for each block of 4 pixels (with the GRBG Bayer pattern), a single RGB pixel is obtained by copying the red and blue and taking a single green value. In other words, the number of pixels is divided by 4. Therefore, the RGB images obtained can be directly compared to generate difference images or error metrics (Mean Absolute Error in this paper). In this way, each RGB channel is represented uniformly by the error metric, which would not be the case if the RAW images were compared (due to the presence of twice as much green in the Bayer pattern). Finally, to display the images, and only for display purposes, a gamma correction ($\gamma = 2.2$) is applied to the photos and renderings.

Spherical Harmonics and Radial Basis Function are used to approximate the measured BRDF values with N coefficients. Empirically, we found that $N = 100$ is a good compromise between computation time and accuracy (Figs. 3 and 4). To avoid *Gibbs phenomenon* induced by SH representation, we apply a window filter that removes strong visual artifacts at the price of a small increase of the MAE error. In contrast, approximation with RBF is more stable but has difficulty reproducing high frequencies accurately. This is illustrated in further detail in the supplemental document [19].

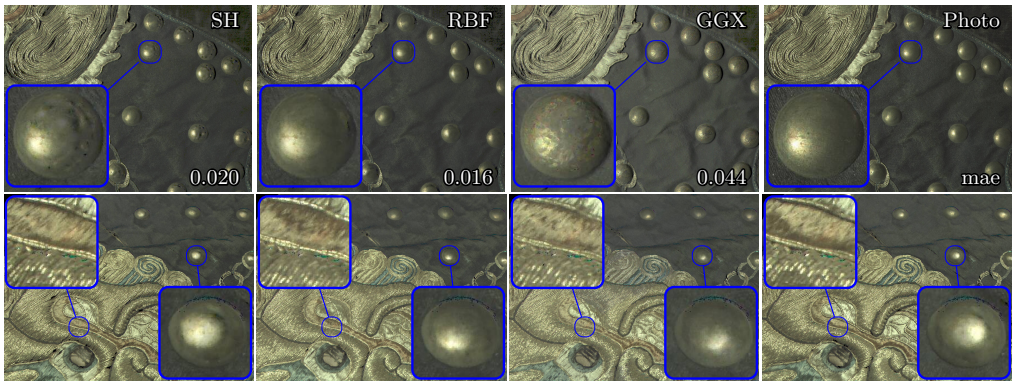

Fig. 5. **Top:** Ablation study where only 50% of the photos are used to approximate the BRDF. In that case, RBF give the lowest MAE and, as illustrated below, they are very stable, in terms of visual appearance, when computing new synthetic images under novel LED positions and orientations. **Bottom:** Four new synthetic images computed using the RBF representation under new (never measured) lighting conditions. A video showcasing other synthetic results is available [29].

GGX BRDF Model tends to generate more errors than the SH and RBF models. This is mainly due to angular uncertainties affecting the directions $\boldsymbol{o}$, $\boldsymbol{i}$ and most importantly the surface normal $\boldsymbol{n}_x$. Unlike SH and RBF, which reconstruct the signal without relying on an explicit normal direction the GGX model is higly sensitive to the accuracy of $\boldsymbol{n}_x$. Even small uncertainties in the estimated normal propagate when transforming the measured samples into the local coordinate system defined by $\boldsymbol{n}_x$. This perturbs the relative angular positions of the samples, whereas the GGX model assumes precise, uncertainty-free orientations to perform optimally. As a consequence, GGX tends to make fabrics appear faded (*cf.* the wedding vest in Fig. 4) and metallic parts appear grainy (*cf.* the Fish skin coat).

Memory cost and timings. Considering a mesh of approximately 500,000 triangles, we generally observe in our datasets that computing the parameters of the SH representation was the fastest, whereas the GGX model was approximately 1.4 times slower and RBFs were twice as slow, but this depends greatly on the number of BRDF measures per triangle. On the other hand, for image reconstruction the GGX model is the fastest, while SH is twice as slow and RBF is six times slower. In terms of memory, the GGX model (with only 7 parameters) is obviously the least expensive, whereas the SH model is $3N/7$ times more expensive. The cost of RBF is similar to SH, with one exception: RBF also requires storing the directions of the radial-based functions. However, as done in this paper, if the directions are the same for all triangles, then this additional cost is negligible. To give an idea, using half a million triangles, GGX represents a cost of 14MB, while SH and RBF represent a cost of 600 MB for $N = 100$.

6.4. Fitting parameters sensitivity

The data processing is guided by several parameters that are more or less tunable by the user. First, a threshold on the theta angle is used to remove samples located at too grazing angles, which tend to generate outliers in the data. However, a threshold of 89° was sufficient in our experiment to remove most of the artifacts. The threshold on the pixel value removes noise and shadows from poorly exposed pixels. We noticed that the RBF and GGX models were particularly robust to this threshold, whereas this is not the case for SH model. We noticed the same trend for the number of photos given as input to the data processing (Fig. 5). Finally, the size of the triangles plays an

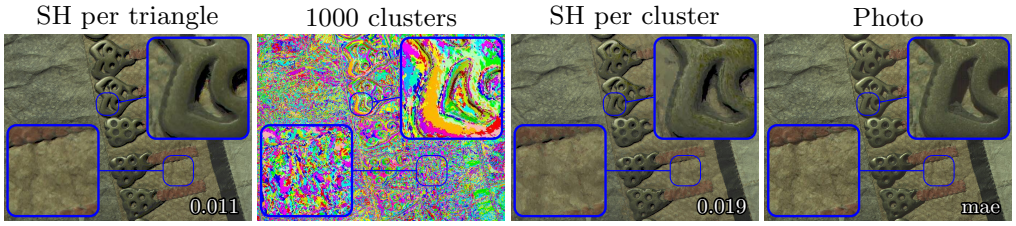

Fig. 6. Segmentation test applying k-means with 1,000 clusters on the SH coefficients per triangle. The samples are then concatenated by cluster to be projected onto the SHs in order to render with only 1,000 SH sets instead of 416,859 in this case. Despite this huge/bug compression factor induced by the clustering, the visual error, reported as MAE, remains very low (0.019 vs. 0.011).

important role in the accuracy of the renderings. Indeed, the smaller the triangles, the greater the spatial accuracy. On the other hand, triangles will tend to collect fewer BRDF samples. While this does not seem to be a particular problem for SH or GGX, it is for RBF, which does not give consistent results when the number of BRDF directions becomes extremely sparse. All these parameters are discussed and illustrated in more detail in the supplemental document [19].

7. Discussion and Future Work

Uncertainties of BRDF radiometric values. As explained in section 6, the positions of the vertices acquired by the 3D scanner are known with an accuracy of 30 µm, which is responsible for 57% of the total BRDF radiometric uncertainty. Using a more recent 3D scanner (20 µm accuracy) would only reduce the overall BRDF median uncertainty from $[-10.66\,\%; +14.00\,\%]$ to $[-8.11\,\%; +9.51\,\%]$. By combining this with a very low-noise camera, such as a Hamamatsu ORCA-Quest 2, our system could achieve a median measurement uncertainty of less than 3.6 %.

Per triangle BRDF data densification. The BRDFs we obtain per triangle are particularly sparse (Fig. 3). Therefore, we would like to densify the BRDFs without necessarily enlarging the initial dataset (*i.e.*, without taking additional photos). Segmentation in BRDF space can be a way to increase data density per triangle. If two triangles are identified as having the same BRDF, the direction samples can be merged to create a more highly sampled BRDF. This would be particularly interesting for the *La Coupole* device, as it has a high spatial density of data (around half a million triangles seen by each photo). However, the uncertainty of the normal $\boldsymbol{n_x}$ poses a major problem for merging BRDF directions from different triangles. Furthermore, automatic segmentation of materials based on sparse measurement data remains a challenge without using an a priori BRDF model. Nevertheless, preliminary tests show encouraging results, with acceptable visual quality achieved by drastically reducing the number of BRDFs (Fig. 6).

Multi-view reconstruction approaches are typically based on a single sensor, which greatly facilitates data calibration and data processing by combining geometry and materials [30, 31] at the price of sacrificing the tracking of the uncertainties of the SVBRDF. In our device, measurement data come from two different sensors: the camera (50 µm resolution) and the 3D scanner (200 µm resolution). Our calibration allows us to realign the photos from two different viewpoints and reproject them on the mesh with maximum precision of one to two millimeters, which corresponds to an offset of around 5-10 triangles (Fig. 7). As future work, we would like to add image-based information to approximate simultaneously the geometry and the SVBRDF while keeping track of the uncertainties. All recent literature on auto-differentiable tools for

Fig. 7. Illustration of the problem of misalignment by projecting photos from different points of view on the mesh. In practice, for the test to be successful, the colored crosses must point exactly to the same features in the photos. Additional results (available in the supplemental document [19]) show that the offset is of the order of ten triangles (approximately 1-2 mm).

rendering could thus be leveraged in this application context [32] but within the limits of the assessed uncertainties above. The optimization process could be made more robust by taking into account other parameters, such as extrinsic camera parameters, at the cost of complexity.

Multi-view reconstruction raises other issues in terms of memory management and continuous representations. For large 3D objects, the cost to export the BRDF samples is around 10 GB of memory per viewpoint. This memory cost becomes redemptive for multiple viewpoints, especially when using RBF or SH representations that need *all* data to provide the best approximation of the SVBRDF. One way to circumvent this memory problem is to compute the RBF or SH representations only for a subset of triangles; however, the processing time will drastically increase since photos need to be read multiple times. In terms of mathematical representations, only SH need to be extended to 4D (*cf.* [33]) to handle multi-view reconstructions. However, the number of required coefficients will increase quadratically for SH. An interesting venue to explore would be to develop a processing pipeline that fetches the data from an image, treats it, and discards it immediately afterward. This will also require a novel and compatible SVBRDF representation.

Progressive acquisition. Currently, data acquisition and reconstruction are two separate processing pipelines that require a significant amount of memory. Furthermore, acquired data may exhibit redundancy. Therefore, merging the two processing pipelines to enable progressive acquisition would allow for better measurement guidance through on-the-fly data processing [34].

8. Conclusion

We have introduced *La Coupole*, a device that combines shape measurements from a 3D Scanner, with optical measurements, from a DLSR camera, to reproduce the appearance of real-world 3D objects. In conjunction with the heterogeneous equipment comprising *La Coupole*, we have also established a comprehensive calibration method and a statistical analysis of the geometric and radiometric uncertainties. Furthermore, we have also compared 3 different continuous representations (SH, RBF, GGX) for SVBRDF approximations and shown that they can reconstruct highly detailed photographs with excellent visual accuracy even in the case of novel lighting configurations.

9. Acknowledgments

This project was supported by the French national research agency project Material (ANR-15-CE38-0005), the region Nouvelle-Aquitaine through the project VESPAA, the European project 23IND14 xDDiff, and the French Ministry of Culture through the project ANIS. Special thanks to Philippe Teulat for his help in designing and manufacturing mechanical parts.

Disclosures. The authors declare no conflicts of interest

See Supplement 1 for supporting content.

References

1. S. R. Marschner, "Inverse rendering for computer graphics," Ph.D. thesis, Cornell University (1998).
2. W. Matusik, H. Pfister, M. Brand, and L. McMillan, "A data-driven reflectance model," ACM Trans. Graph. **22**, 759–769 (2003).
3. M. Weinmann and R. Kleiny, "Advances in geometry and reflectance acquisition (Course Notes)," in *SIGGRAPH Asia 2015 Courses, SA 2015,* (Association for Computing Machinery, Inc, 2015).
4. D. Guarnera, G. C. Guarnera, A. Ghosh, *et al.*, "BRDF representation and acquisition," Comput. Graph. Forum **35**, 625–650 (2016).
5. D. K. McAllister, "A generalized surface appearance representation for computer graphics," thesis, Chapel Hill p. 129 (2002).
6. M. Sattler, R. Sarlette, and R. Klein, "Efficient and realistic visualization of cloth," in *Proceedings of the 14th Eurographics Workshop on Rendering,* (Eurographics Association, 2003), EGRW '03, pp. 167–177.
7. V. Havran, J. Hošek, Š. Němcová, *et al.*, "Lightdrum—Portable light stage for accurate BTF measurement on site," Sensors (Switzerland) **17** (2017).
8. M. Holroyd, J. Lawrence, and T. Zickler, "A coaxial optical scanner for synchronous acquisition of 3D geometry and surface reflectance," ACM SIGGRAPH 2010 Pap. SIGGRAPH 2010 **29**, 1 (2010).
9. C. Schwartz, M. Weinmann, R. Ruiters, and R. Klein, "Integrated High-Quality Acquisition of Geometry and Appearance for Cultural Heritage," in *The 12th International Symposium on Virtual Reality, Archeology and Cultural Heritage VAST 2011,* (2011), pp. 25–32.
10. C. Schwartz, R. Sarlette, M. Weinmann, and R. Klein, "DOME II: a parallelized BTF acquisition system," Workshop on Material Appear. Model. (2013) pp. 25–31 (2013).
11. J. Kohler, T. Noll, G. Reis, and D. Stricker, "A full-spherical device for simultaneous geometry and reflectance acquisition," in *Proceedings of IEEE Workshop on Applications of Computer Vision,* (2013), pp. 355–362.
12. E. Garces, V. Arellano, C. Rodriguez-Pardo, *et al.*, "Towards Material Digitization with a Dual-scale Optical System," ACM Trans. on Graph. (Proc. SIGGRAPH) **4** (2023).
13. J. Baron, X. Li, P. Joshi, *et al.*, "VarIS: Variable Illumination Sphere for Facial Capture, Model Scanning, and Spatially Varying Appearance Acquisition," in *Smart Tools and Applications in Graphics - Eurographics Italian Chapter Conference,* (The Eurographics Association, 2023).
14. G. Nam, J. H. Lee, D. Gutierrez, and M. H. Kim, "Practical svbrdf acquisition of 3d objects with unstructured flash photography," ACM Trans. Graph. **37** (2018).
15. M. Tetzlaff, "High-fidelity specular svbrdf acquisition from flash photographs," IEEE Trans. on Vis. Comput. Graph. **30**, 1885–1896 (2024).
16. K. E. Torrance and E. M. Sparrow, "Theory for off-specular reflection from roughened surfaces∗," J. Opt. Soc. Am. **57**, 1105–1114 (1967).
17. F. E. Nicodemus, J. C. Richmond, J. J. Hsia, *et al.*, *Geometrical Considerations and Nomenclature for Reflectance* (National Bureau of Standards, 1977).
18. J. Arvo, "Applications of irradiance tensors to the simulation of non-lambertian phenomena," in *Proceedings of the 22nd Annual Conference on Computer Graphics and Interactive Techniques,* (1995), SIGGRAPH '95, p. 335–342.
19. A. Lucat, P. Mézières, F. Margall, *et al.*, "La coupole: A svbrdf measurement device for large and non-planar objects: Supplemental document," https://people.bordeaux.inria.fr/romain.pacanowski/lacoupole/lacoupole_supp.pdf (2025).
20. Z. Zhang, "A flexible new technique for camera calibration," Tech. Rep. 11, Microsoft Research (2000).
21. O. Authors, "Opencv pinhole camera model," https://docs.opencv.org/4.x/d9/d0c/group__calib3d.html (2025).
22. R. Horaud and F. Dornaika, "Hand-Eye Calibration," Technical report (1994).
23. B. Walter, S. R. Marschner, H. Li, and K. E. Torrance, "Microfacet models for refraction through rough surfaces." Render. techniques **2007**, 18th (2007).
24. P.-P. Sloan, "Stupid spherical harmonics (sh) tricks," Game Dev. Conf. **9**, 320–321 (2008).
25. R. L. Cook and K. E. Torrance, "A reflectance model for computer graphics," ACM Trans. Graph. **1**, 7–24 (1982).
26. G. Guennebaud, B. Jacob *et al.*, "Eigen v3," http://eigen.tuxfamily.org (2010).
27. J. Löw, J. Kronander, A. Ynnerman, and J. Unger, "Brdf models for accurate and efficient rendering of glossy surfaces," ACM Trans. Graph. **31** (2012).
28. ISO/IEC, "Propagation of distributions using a Monte Carlo method," Tech. Rep. 98-3:2008/Suppl 1:2008 (2008).
29. A. Lucat, P. Mézières, F. Margall, *et al.*, "La coupole : relighting," https://youtu.be/sfWFZEBeWp4 (2025).
30. B. Kerbl, G. Kopanas, T. Leimkühler, and G. Drettakis, "3d gaussian splatting for real-time radiance field rendering." ACM Trans. Graph. **42**, 139–1 (2023).
31. M. Tetzlaff, "High-fidelity specular svbrdf acquisition from flash photographs," IEEE Trans. on Vis. Comput. Graph. **30**, 1885–1896 (2023).
32. C. Zhang, B. Miller, K. Yan, *et al.*, "Path-space differentiable rendering," ACM Trans. Graph. **39**, 143:1–143:19 (2020).
33. C. Soler, M. M. Bagher, and D. Nowrouzezahrai, "Efficient and accurate spherical kernel integrals using isotropic decomposition," ACM Trans. Graph. **34** (2015).
34. R. Wiersma, J. Philip, M. Hašan, *et al.*, "Uncertainty for svbrdf acquisition using frequency analysis," in *Proceedings of the SIGGRAPH Conference Papers,* (2025), pp. 1–12.